ISSN 1054-660X, Laser Physics, 2011, Vol. 21, No. 11, pp. 1962–1971.
© Pleiades Publishing, Ltd., 2011.
Original Text © Astro, Ltd., 2011.

Can Temporal Analysis of Optical Coherence Tomography Statistics Report on Dextrorotatory-Glucose Levels in Blood?[1]

H. Ullah[a, b, *], A. Mariampillai[c], M. Ikram[a], and I. A. Vitkin[b]

[a] *Department of Physics and Applied Mathematics, Pakistan Institute of Engineering and Applied Sciences, Islamabad, Pakistan*

[b] *Department of Medical Biophysics and Radiation Oncology, University of Toronto, and Division of Biophysics and Bioimaging, Ontario Cancer Institute/University Health Network, Toronto, Ontario, Canada*

[c] *Department of Electrical Engineering, Ryerson University, Toronto, Ontario, Canada*

*e-mail: hafeezullah79@gmail.com

Received April 26, 2011; in final form, May 2, 2011; published online September 2, 2011

Abstract—We report the use of optical coherence tomography (OCT) for measuring dextrorotatory-glucose (D-glucose) in liquid phantoms and in drawn blood based on temporal dynamics of light scattering. The presence of D-glucose alters the medium viscosity, thus affecting the Brownian motion of the scatterers (polystyrene microspheres (PMS) in phantoms, red blood cells (RBCs) in blood) as measured by OCT. To quantify the effect, the signal autocorrelation functions were measured from M-mode OCT data and exponentially fit to obtain the decorrelation times. These were then related to translational (and rotational, in case of asymmetric scatterers) diffusion coefficients which enabled the determination of D-glucose-controlled medium viscosity. Obtained viscosily values agreed well with the literature, and showed expected increase with D-glucose concentrations. Whole blood smears were imaged with microscope and another effect of added glucose, that of red blood cell deformation, was also observed. This phantom and blood OCT study demonstrates the technique's ability to detect and quantify D-glucose presence in non-flowing liquid suspensions, and suggests several additional research routes necessary to determine its potential for in vivo applications.

DOI: 10.1134/S1054660X11190285

1. INTRODUCTION

Diabetes is a common and debilitating disease whose incidence is currently on the increase. Diabetic patients experience dramatic swings in blood D-glucose concentrations, which can lead to both acute emergencies and long-term complications. Much effort has gone into developing methods for non-invasive monitoring and quantification of D-glucose levels, such that diet, exercise, and insulin therapies can be administered in an optimal fashion. However, this has proven to be an exceedingly difficult problem, owing to relatively small physiological levels of D-glucose, abundance of other confounding analytes, variability in patient physiology, difficulties in direct measurement, sampling volume ambiguities, and other problems. Nevertheless, driven by the outstanding clinical need and significant commercial possibilities, much academic and industrial activity in this field continues. In addition to the outstanding problem of glucose measurement in diabetes, noninvasive techniques to measure other biological analytes and their diffusion dynamics are needed in several other important clinical scenarios [1].

Lasers for many years have been used for in vitro and in vivo study of biological tissues. In diabetes the lasers have no harm full for diagnostics sugar levels in patients [2]. Particular techniques investigated for noninvasive glucose detection include metabolic heat conformation studies [3], optical absorption and scattering methods, near and mid-infrared spectroscopy, Raman spectroscopy, photoacoustic spectroscopy, light polarimetry, spectrophotometry, spectrofluorometry, microdialysis and laser Doppler approaches, X-rays, computed tomography (CT), magnetic resonance imaging (MRI) and single-beam Z-scan technique, all with their unique own set of advantages and disadvantages [4, 5]. For example, the Z-scan technique attempts to quantify glucose levels in blood based on the induced non-linear refractive index changes, but the method is applicable only in transmission mode. The limitations include measurement of glucose level in a patient where only scattering is possible because light especially 520 nm cannot pass through a normal human body [6]. X-rays used in CT scanning can be harmful for patients; MRI's measurements of relaxation times can be linked to blood glucose levels but may be problematic in terms of imaging resolution; in any case, MR1 and CT are big and expensive installations that are not suitable for home, patient-oriented use than an ideal noninvasive glucose sensor should be used.

As evident from the above list, much of the research in gluocometry has been in the field of biophotonics, owing to light's many attractive characteristics for noninvasive analyte determination and the compact/portable/inexpensive nature of the associated

[1] The article is published in the original.

technology. Of these, optical coherence tomography (OCT) is particularly promising. Using the principles of optical interferometry and coherence gating, OCT can yield micron-scale resolution subsurface images of tissues, with high sensitivity to details of biological structures/analytes that influence its measured back-scattering signal [7–9]. The technique is attractive for real time in situ imaging approaching the limits of conventional histology (but without the need for tissue excision!), with penetration depth of 1–3 mm in most tissues, and with access to many body sites enabled by fiber optics implementation [10]. OCT's limitations include strong scattering of probing light from the biological tissues at the visible and near infra red (NIR) wavelengths, yet this is spectral range available for biophotonic diagnosis as dictated by the constraints of tissue optics. Glucose can act as optical clearing or dehydration agent to increase the imaging depth and causes in reduction of refractive index mismatch. Hence, this refractive index mismatch causes the formation of RBCs aggregation in whole blood [11]. Whether OCT can reliably measure blood glucose levels in vivo (~1 gmol of glucose in a liter of blood for normal physiology (~5–6 mM), and 3–25 mM fluctuations in diabetics) remains an open question. Several OCT studies are attempting to quantify tissue scattering changes driven by the glucose-induced refractive index matching effect [11–14]. Here, we investigate an alternative use of OCT for glucometry, by concentrating on glucose-induced changes in blood viscosity.

We report initial results and analysis using M-mode OCT to measure medium viscosity η from a specific depth within a non-flowing liquid medium. This approach may be applicable for in vivo applications, both in the research and clinical diabetes settings. As alluded to above, glucose presence is known to change tissue scattering characteristics by the so-called refractive index matching effect in the extra-cellular fluid (increasing its refractive index by ~0.0273 per mole of glucose [14], and this effect has been exploited in several light-scattering based techniques [15], including OCT [11, 13]. In this pilot study, we report quantification of D-glucose diffusion in water, blood plasma and in vitro whole blood from a normal rat based on the corresponding changes in liquid viscosity using swept source (SS)-OCT [16]. Specifically, the D-glucose-induced changes in medium viscosity were derived from the OCT measurements of relaxation times of scattering particles PMS in water and in blood plasma, and RBCs in whole blood. This research builds on our recently developed speckle-variance OCT method to delineate tissue micro vasculature in-vivo based on different temporal speckle decorrelation characteristics between "solid" and "liquid" components of biological tissues [17]; here, we report on initial fundamental studies to further elucidate this source of contrast and to investigate its sensitivity to varying D-glucose levels in liquid phantoms and in drawn blood samples. Here we investigate the OCT's ability to quantify the glucose diffusion process by analyzing stokes Einstein's law in Brownian motion. [18]. The whole research work was done at Princess Margret Hospital/Ontario Cancer Institute/University Health Network/Department of Medical Biophysics, University of Toronto, Toronto, Canada.

Dynamic light scattering (DLS) based on phase and/or amplitude fluctuations of singly-scattered light detects scattering particle dynamics, and can be used to study their structural and dynamical properties [19]; some initial OCT research has previously exploited this route. OCT based on DLS can quantify exponentially attenuated signals due to spherical scatterer's relaxation, as OCT signal arises primarily from singly scattered (ballistic) light. The transition to multiply scattering regime, so called diffusing wave spectroscopy (DWS), has also been discussed [19]. DWS is applicable for multiple scattering where information is collected from more depth [20]. While such phantom demonstrations based on spherically symmetrical scatterers have been performed, the situation is more complex for asymmetric scattering particles (such as RBCs with their biconcave disk shape). Here, relaxation (and thus temporal decorrelation dependence of the resultant OCT signal) occurs not only by translational Brownian motion as the case for spheres, but also via rotational relaxation. Although some analytical hydrodynamic solutions for such anisotropic diffusion of asymmetrical particles have been reported, the situation is not as clear-cut as for symmetric spheres, and ambiguities in results interpretation exist due to diffusion motion complexity. For example, saucer-like dynamics are expected in the direction of a transverse axis of an ellipsoid of revolution (~translation), while axis tumbling can change the orientation (~rotation); both motions can influence the signal decorrelation times as measured by light scattering techniques [21]. An additional issue with blood scattering is that RBCs are also deformable, for example changing their shape depending on osmotic pressure fluctuations [22].

It was necessary to see the deformation/aggregation of cells with respect to glucose addition [23]. Hence, we have imaged the rouleaux formation with the help of light microscope which provides efficient visualization of RBCs after glucose admixing in blood.

Further, in an in-vivo setting in the context of flowing blood, other complicating effects come into play, such as rouleaux cooperative motion and motion-induced deformations [24]. The situation is clearly complex, and controlled systematic studies are required to determine if D-glucose-induced viscosity changes can indeed be detected and quantified by temporal analysis of OCT signal fluctuations. This paper reports on the first step in such systematic studies; deformations of RBCs are also analyzed with the help of light microscopy. Specifically, we use M-mode OCT to quantify D-glucose-induced alterations in non-flowing liquid settings of increasing complexity,

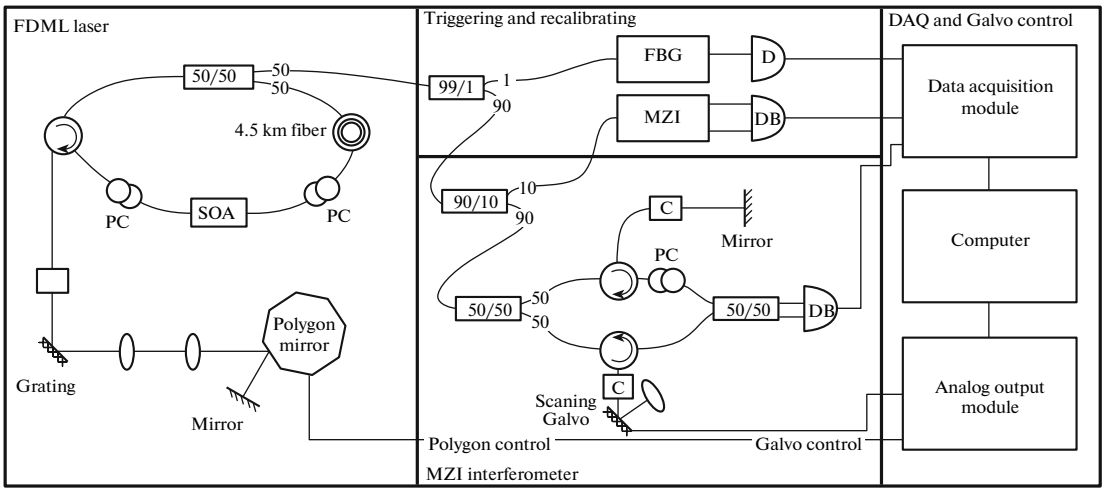

Fig. 1. Conceptual diagram of FDML SS-OCT system. In this schematic, SOA: semiconductor optical amplifier, PC: polarization controller, C: collimator, FBG: fiber Bragg grating, MZI: Mach–Zender interferometer, D: detector, DB: dual balanced detector [32]..

consisting of: (1) symmetrical (spherical-scatterers) water phantoms; (2) symmetrical (spherical-scatterers) blood plasma phantoms; and (3) asymmetrical-scatterers (RBC) whole blood samples. In each case, we measure temporal decorrelation dynamics by extracting the relaxation times, relate these to diffusion coefficients, and calculate the resultant medium viscosities. Potential in-vivo D-glucose monitoring implications of these findings, in the context of our recently developed speckle-variance OCT approach for microvascular tissue imaging [17], are briefly discussed.

2. MATERIALS AND METHODS

2.1. Samples

Three types of scattering samples with varying D-glucose concentrations were used in this investigation:

(1) The first set was water phantoms with 1.4 μm diameter PMS and six different concentrations of D-glucose (0, 100, 200, 300, 400, and 500 mM). The microsphere concentrations increased from 0.69% (weight/volume) for D-glucose-free suspension to 0.76% for the 0.5 mM phantom, in order to keep the scattering coefficient μ_s constant in the presence of the refractive index matching effect [15]. Assuming the refractive index of water ~1.33, μ_s was calculated from Mie theory at 1310 nm to be 100 cm^{-1} [25, 26]. These phantoms served as the "simplest" control set in having constant scattering properties engendered by spherically symmetric scatterers. The further investigation of scattering effect due to glucose addition is suggested to be analyzed with diffuse reflectance. The deformation in biological tissues due to addition of glucose can be visualized with speckle variance OCT [27, 28].

(2) The next experimental series was a symmetric scatterer set (PMS as in (1)) suspended in blood plasma instead of water. Whole blood was drawn from five months old female Fisher rats into heparin tubes which were then centrifuged to separate out the plasma. To these plasmas we added a fixed concentration 0.0073% of 1.4 μm diameter PMS and varying D-glucose amounts (0, 80, 160, 240, 320, and 400 mM). Here, our Mie scattering calculations assumed a refractive index value ~1.34 for rat plasma, extrapolated from previously-reported $n \sim 1.35$ at 630 nm for human blood plasma [11, 29]. In this sample set, we did not increase the PMS concentration with added glucose amounts, thus the scattering coefficient decreased with increasing refractive index matching effect (100 cm^{-1} with no added glucose, to ~ 70.7 cm^{-1} at the highest added glucose concentration of 400 mM) [25, 26]. This was done deliberately to simulate similar effects in whole blood phantoms.

(3) Finally, asymmetric RBC scatterers in the natural blood environment were investigated. Similar to (2), whole blood drawn from five months old Lewis rats was admixed with additional D-glucose to 0, 20, 40, 60, and 80 mM levels. Note that these added glucose levels are lower than those in sets (1) and (2), and are indeed closer to the human physiological levels mentioned above; this too was done on purpose to better gauge the applicability of this approach to eventual in-vivo situation.

2.2. Measurement System

A custom built 36 kHz SS-OCT system was used for M-mode scanning similar to that described previously, as shown schematically in Fig. 1 [17, 30–32]. Briefly, the SS-OCT system consists of frequency

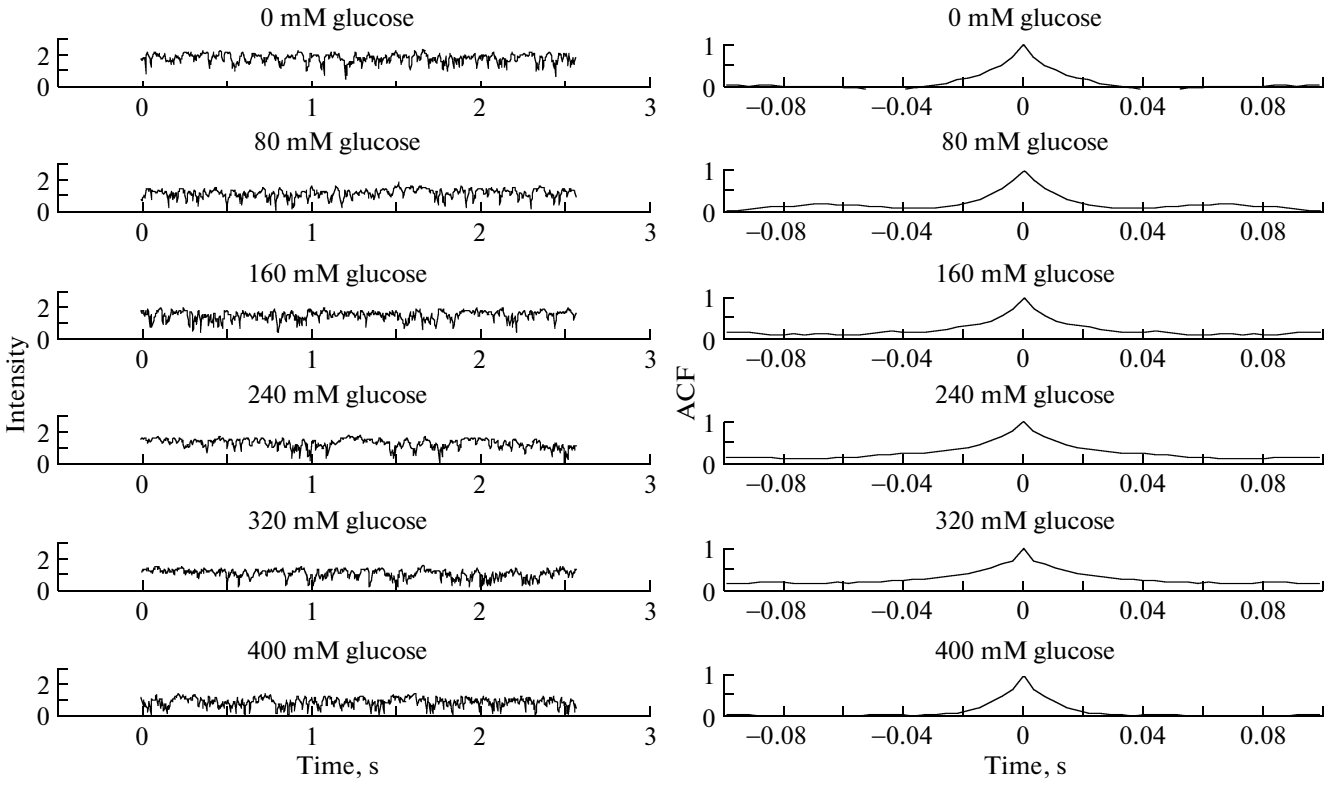

Fig. 2. (a) OCT M-mode intensity signals at a depth of 70 μm for six different D-glucose concentrations in the blood plasma + PMS phantom set (2) at 21°C. (b) Signal autocorrelation functions (*ACF*) obtained from the OCT M-mode data of (a), via Eq. (2). *ACF* curves exhibit exponential decay, which is characteristic of Brownian motion of the scatterers. Slower relaxation is seen in samples with higher D-glucose concentration.

domain mode locking (FDML) fiber-ring laser source comprising of polygon-based tunable filter. The FDML configuration consists of total cavity length of 3.3 to 4.5 km. A fiber Bragg grating is used for A-scan triggering. The coherence length and spectral sweeping range were 6 mm and 112 nm, respectively, at a central wavelength of 1310 nm. The axial resolution in tissue and the average output power of the system were 8 μm and 48 mW. Hence, this phase sensitive SS-OCT can be coupled to take into account motion artifacts in speckle variance OCT for mapping blood vessels on the basis of glucose induction and quantification [33, 34].

To perform M-mode analysis, we chose to analyze the OCT signal intensity 70 μm below the liquid sample surface; this depth is free any possible surface distortions or artifacts, and not deep enough to invoke complications and signal distortions caused by multiple scattering [19]. To obtain M-mode data, we repeatedly acquired full depth (~2 mm) A-scans for ~5 s at the same central sample lateral location, averaged 64 consecutive A-scans, and plotted this average signal intensity at our selected 70 μm depth as a function of time. For illustrative purpose Fig. 2a shows raw OCT M-mode intensity signals at a depth of 70 μm for six different D-glucose concentrations in the blood plasma + PMS phantom set (2) up to ~2.5 s. The resultant data train consists of ~1400 OCT intensity points 3.6 ms apart. As viscosity is a temperature-dependent quantity, care was taken for all the three phantom sets to perform the OCT measurements at a fixed temperature of 21°C.

To explore possible shape changes of RBC with the addition of glucose, we used an inverted motorized microscope (Zeiss Axio–Observer), as shown in Fig. 3. RBCs biconcave shapes with their equilibrium diameter of ~7 μm can be readily observed with this set-up. Additional microscope features such as multichannel, time lapse, and Z-stacking can help in further sample visualization, including 3D shape information. For these studies, whole blood smears from sample set (3) were placed on standard microscope glass slides and examined in transmission mode under 40X magnification [35]. For therapy point of view, cells deformation measurements have received important intention from many researchers, for example, human umbilical cord derived mesenchymal stem cells's (hUC-MSCs) viability transitions is critical from quality control and their population expansion [36].

Fig. 3. Axio-observer inverted motorized microscope used to image RBCs in whole blood smears for different glucose concentrations [35].

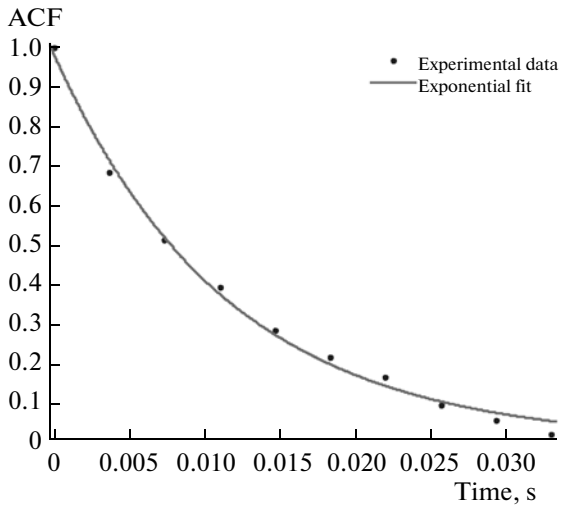

Fig. 4. A typical exponential fit to *ACF* data for extraction of decorrelation times ($r^2 = 0.99$). The AFC is from the "0 mM" PMS + plasma sample (set (2)), yielding $\eta_{plasma} = 1.16$ mPa s from Eq. (3).

2.3. Signal Processing

The signal recorded at the detector of the OCT system is given by [37]

$$I_D = \frac{1}{2}\int_0^\infty I_{SO}(k)(1+\cos kx)dk = \frac{1}{2}I_{SO} + \frac{1}{4}\int_{-\infty}^{\infty} I_{SO}(k)e^{ikx}dk, \quad (1)$$

where x is the path length difference, $I_{SO}(k)$ is the source intensity and the integral $\int_0^\infty I_{SO}(k)e^{ikx}dk$ is called autocorrelation function (*ACF*). The power spectrum $P(\omega)$ and *ACF* are related by Weiner–Khinchin theorem as a Fourier pair:

$$P(\omega) = \left|E(\omega)^2\right| = \int_{-\infty}^{\infty} ACF(t)e^{i2\omega\tau}d\tau \quad \text{or} \quad ACF(x) = \int P(\omega)e^{-i\omega x/c}d\omega. \quad (2)$$

Figure 2a shows representative OCT intensity signals as a function of time (M-mode) at a depth of 70 μm for six different D-glucose levels c_{gl} in plasma + PMS phantom (sample set (2)). As described, we combined 64 consecutive A-scans at the pre-selected 70 μm depth to yield one M-mode point, resulting in ~3.6 ms spacing on the time graphs of Fig. 2a. The *ACF* was extracted according to Eq. (2), processed using Matlab. Figure 2b illustrates the *ACF* for the six different c_{gl} in blood plasma. It is seen that increasing D-glucose levels cause longer OCT signal relaxation decays, as expected from the slower Brownian motion of scattering particles in media of increasing viscosity. Although there were ~1.400 data points over the 5 s signal acquisition, about half (2.5 s, 700 points) are shown for clarity in Fig. 2a. As seen from 2b, ~280 points (0.1 s) are plotted, as sufficient for the *ACF* decay analysis. The difference in the decay can be observed very carefully because the decay time interval, $\Delta\tau$ is in the range of milliseconds.

To quantify these effects, two distinct signal decorrelation mechanisms must be considered for scattering particles undergoing Brownian motion: translation and rotation. For spherically symmetric shapes such as PMS, only the former mechanism applies; for asymmetric RBCs, both mechanisms must be considered. The analysis for sample sets (1) and (2) is thus somewhat simpler, and we examine that first.

A single exponential fit function $f_1 = A\exp(-t/\tau_T)$ was applied to each *ACF* to extract the translational decorrelation time τ_T. Figure 4 shows a typical exponential to the plasma + PMS sample prior to D-glucose addition. The point selection for this fit was fixed up to decay of the signal to ~zero amplitude; the data points beyond this limit were in the noise level and thus were not used in the fitting procedure. The high values of the goodness-of-fit metric, the correlation coefficient r^2, was typically ~0.98 for samples in sets (1) and (2) (range 0.94–0.99), indicating that the data is well described by the proposed mono-exponential decay relationship. Translational decorrelation time τ_T thus derived is related to the translational diffusion

Summary of the OCT experimental results and analysis for the three phantom sets, demonstrating the quantification of D-glucose-induced viscosity changes

Sample D-glucose concentration, mM	Translational decorrelation time, ms	Viscosity: from Eq. (3) for sets (1) and (2); from Eq. (4) for set (3), mPa s	r^2-value
Phantom set (1)—single exponential fit			
0	8.77 ± 0.04	0.88	0.97
100	9.25 ± 0.06	0.93	0.98
200	10.21 ± 0.06	1.03	0.98
300	11.20 ± 0.10	1.13	0.99
400	12.20 ± 0.06	1.24	0.97
500	14.10 ± 0.05	1.44	0.95
Phantom set (2)—single exponential fit			
0	11.46 ± 0.14	1.16	0.99
80	12.27 ± 0.16	1.25	0.99
160	15.70 ± 0.12	1.60	0.98
240	21.12 ± 0.21	2.17	0.97
320	26.4 ± 0.16	2.72	0.94
400	44.1 ± 0.29	4.61	0.99
Phantom set (3)—double exponential fit*			
0	8.20 ± 0.04	9.03	0.93
20	9.52 ± 0.08 (8.41 ± 0.04)	10.26	0.99
40	12.00 ± 0.05 (10.40 ± 0.06)	10.81	0.91
60	26.30 ± 0.13 (12.20 ± 0.06)	24.61	0.93
80	63.00 ± 0.40 (25.00 ± 0.14)	51.05	0.99

Note: * For the blood samples, the bracketed decorrelation times represent measurement baseline drift due to blood exposure to air, in the absence of D-glucose aliquots (see text for details). We corrected for this prior to using Eq. (4) to derive the displayed viscosity values in column (3), via τ_T' (corrected) = τ_T' (0 mM) + (difference between the τ_T' values in column (2)).

coefficient D_T, which in turn is dependent on medium viscosity. For spherical scatterers of radius R, the governing equations are [21]

$$\tau_T = \frac{1}{2k^2 D_T} \quad \text{and} \quad D_T = \frac{k_B T}{6\pi\eta R}, \tag{3}$$

where $k = 4\pi n/\lambda$ is wave number, n is the refractive index, k_B is Boltzmann constant, T is absolute temperature, and η is the viscosity of the medium. The latter quantity can thus be obtained from the known values in Eq. (3) and experimentally derived values of translational decorrelation times τ_T for sample sets (1) and (2).

To analyze the whole blood results with its asymmetric RBCs (sample set (3)), a double exponential fit to account for both translational and rotational relaxations was applied to the OCT's ACFs. A simple functional form $f_2 = B\exp(-t/\tau_T') + C\exp(-t/\tau_R)$ was used, where τ_T' and τ_R are the translational and rotational decorrelation times of erythrocytes. To ensure that a double exponential decay was indeed the proper description of the whole blood data, its r^2 values were compared with those from single exponential fits. The resulting correlation coefficient values of ~0.95 were significantly larger that the $r^2 \sim 0.8$ for the single exponential fit to the blood data, strongly suggesting that both translational and rotational are indeed occurring in (3). For comparison, note that a single exponential fits the data well ($r^2 \sim 0.97$) for sample sets (1) and (2) that contain spherical PMS scatterers. However, the translational and rotational decorrelation times thus derived are difficult to relate to their respective diffusion coefficients: because of the complex biconcave disk shape of RBCs, no exact analytical expression exists. If we approximate RBCs as a flattened ellipsoid of radius R and half the average thickness a, in analogy with Eq. (3) there results [21]

$$\tau_T' = \frac{1}{2k^2 D_T'} \quad \text{and} \quad D_T' = \frac{k_B T}{6\pi\eta a} G(\rho), \tag{4}$$

where G is a geometrical factor given by $G(\rho) = (\rho^2 - 1)^{1/2}\rho\arctan(\rho^2 - 1)$ and $\rho = R/a > 1$. For a red blood cell, $R \sim 3.5$ μm and $a \sim 1.0$ μm [38]. The corresponding rotational relaxation analysis could have been sim-

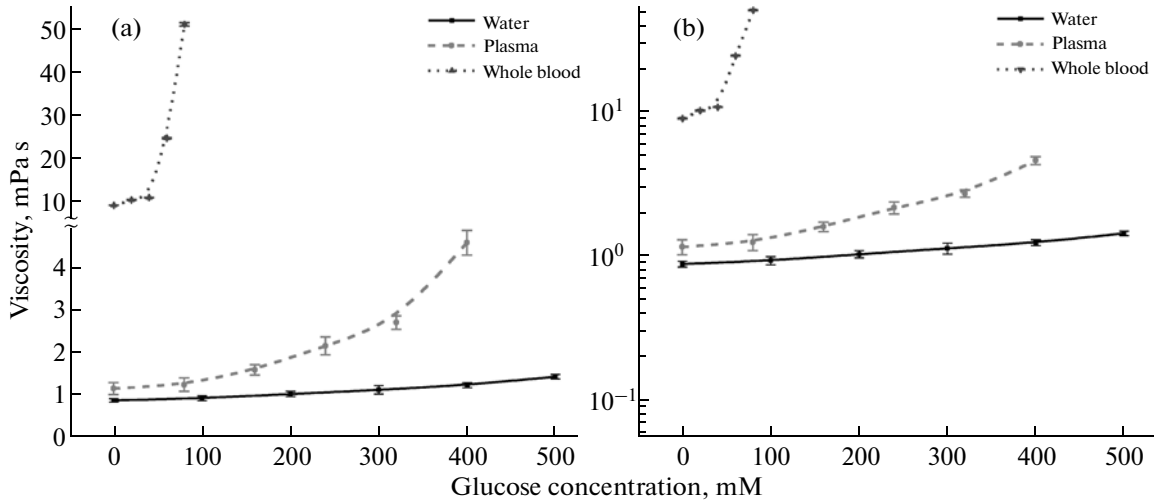

Fig. 5. Viscosities of water and plasma phantom sets (with PS microsphere scatterers, analyzed via Eq. (3)), and of whole blood (with RBC scatterers, analyzed via Eq. (4)). (a) Linear scale, (b) semi-logarithmic scale, showing exponential dependence of viscosity on D-glucose levels in water and plasma systems, and a more complicated (supra-exponential) behavior in whole blood. Symbols are the results of experimental measurements (with errors bars = standard deviations), the lines are a guide for the eye.

ilarly pursued for another estimate of medium viscosity. However, we chose not to do so at present, as relating experimentally derived values of τ_R to medium properties for such scattering shapes is even less certain than the translational relaxation analysis of Eq. (4). Thus, while performing a double exponential fit and obtaining both translational and rotational decay times in whole blood, only the former results are further analyzed to yield medium viscosity as per Eq. (4). Future work will evaluate the information content of the obtained τ_R values. For now, we examine the B/C ratio to estimate the relative importance of translational versus rotational relaxation. For the five blood samples of experimental set (3), this ratio was ~2.7, indicating that translational decorrelation is somewhat more important than rotational relaxation.

3. RESULTS AND DISCUSSION

Table summarizes the quantitative study findings. For the three sets of samples of varying added dissolved D-glucose concentrations, the derived translational decorrelation times τ_T for (1) and (2), the derived translational decorrelation times τ_T' for (3), the resulting viscosities η, and the fitting correlation coefficients r^2 are given. Also included in brackets are the decorrelation time results of a control experiment in the data set of blood sample set (3); here, we were concerned with possible confounding D-glucose-independent effects of long exposure of blood to the air during the measurements of increasing D-glucose aliquots, and thus admixed saline-only amounts throughout the corresponding time course of another OCT blood measurement experiment. This would account for the possible measurement baseline drift.

Concentrating initially on phantom set (1), the D-glucose-free water + PMS sample yields a viscosity $\eta_{water} = 0.88$ mPa s. This is in fairly good agreement with the accepted textbook value of 0.98 mPa s at 20°C [39]. The slight 10% discrepancy is likely due to imprecise experimental temperature control, as viscosity is known to be highly temperature dependent. Another possible reason may be PMS themselves, in that their presence effectively changes the viscous properties of the water suspension, but at the ~0.7 vol % loading this is unlikely to be a major effect. We are currently refining our apparatus and analysis to enable better results accuracy. Moving on to the D-glucose-containing PMS suspensions of set (1), a trend of increasing viscosity is observed. This increase makes sense, and its magnitude seems commensurate with the significant levels of added D-glucose. Comparing with literature, our derived viscosity value of 1.44 mPa s for the 500 mM sample (9 wt %) is in reasonable agreement with the previously-reported $\eta = 1.24$ mPa s for 10 wt % glucose solution [40]. The results are graphically represented with solid line in Fig. 5a.

The plasma + PS phantom set (2) results exhibit a similar trend to the water + PS phantoms, with decorrelation times and viscosity values increasing with the addition of D-glucose. Note that here, the "0 mM" sample does not imply glucose-free medium as in sample set (1), since there is some normal base level of D-glucose present in the plasma (and in whole blood of sample set (3)). Its baseline viscosity is of 1.16 mPa s ~28% higher than that of water, and agrees reasonably well with literature values of 1.29 mPa s [41]. Comparing the η_{plasma} glucose dependence to water-based results as displayed in Fig. 5a, a slightly higher increase in viscosity is seen. The overall increasing viscosity

trends, however, are similar for the two PMS-containing phantom sets.

Finally, it is encouraging to observe that despite the many complexities associated with whole blood analysis (phantom set (3)), our results also show increasing medium viscosity with added D-giucose levels. As discussed above, only translational relaxation times were used in the viscosity determination; ongoing work is exploring the optimal route for rotational relaxation times analysis. Not surprisingly, blood is seen to be "thicker than water", as the derived viscosity value for the blood sample without added D-glucose is ~8 times that of water (9.03 mPa s versus 0.88 mPa s). This η_{blood} static value also agrees well with the literature, where a value of ~10 mPa s is reported [42, 43]. It is seen that the addition of D-glucose to whole blood has a more drastic change on derived medium viscosity compared to either water or plasma, although blood is a non-Newtonian fluid (Fig. 5b). In literature, the viscosity of the blood is quoted in increasing trend with increase in the dextran concentrations [44]. Since the addition of D-glucose also changes the shape of the erythrocytes due to modulations in the osmotic pressure, the resultant scatterer shape change makes it unclear if the data analysis embodied in Eq. (4) holds equally true across the examined D-glucose concentration range. Thus, although the significant increase in the relaxation times and thus in the derived viscosity values is qualitatively correct, its quantification in terms of derived viscosity values is less certain. Also, the magnitude of the confounding effect of long air exposure, as quantified in a control blood measurement experiment with sham (D-glucose-free) saline aliquots (results in parenthesis in table), while certainly smaller than D-glucose, is not insignificant. Better methods to minimize this measurement artifact will be investigated in future publications. The D-giucose-induced viscosity changes in whole blood, corrected for the measurement baseline drift, are also plotted in Fig. 5a.

It is interesting to further examine the D-glucose-induced viscosity increases displayed by the three plots in Fig. 5a. Figure 5b re-plots the data on a semi-logarithmic scale to check if the medium viscosities depend on the D-glucose concentrations in an exponential way. As seen, this indeed appears to be so for the water and approximately so for the plasma samples containing PMS as symmetrical scatterers; the dependence is more complicated (and supra-exponential) in the case of blood. This is perhaps not surprising, given the complex nature of blood milieu—viscosity changes, irregular RBC shape and its alterations, exposure to air complications, possible RBC aggregations, and so on. Thus, even though OCT decorrelation times can be reliably measured, unambiguously and quantitatively relating these to medium viscosities (and hence to D-glucose level) poses significant challenges and necessitates further research.

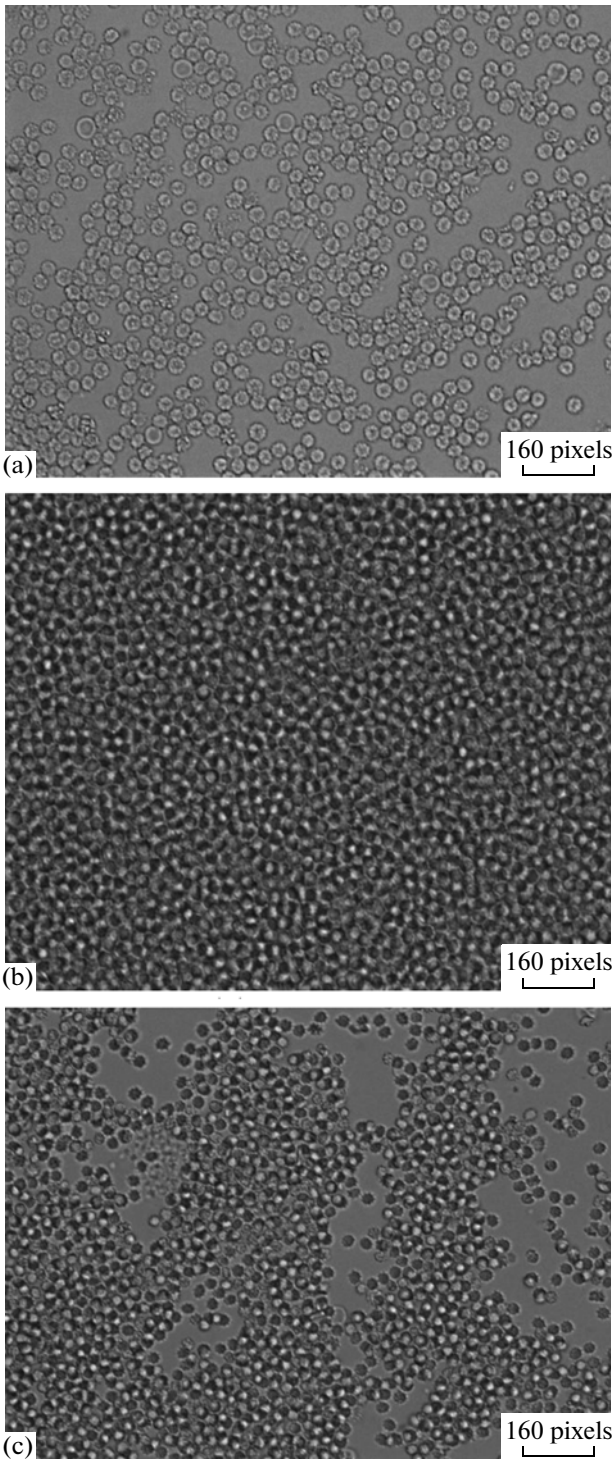

Fig. 6. Microscopy results demonstrating deformation and rouleaux formation of RBCs in rat whole blood samples with the addition of D-glucose. (a) no D-glucose added, (b) 20 and (c) 40 mM. The shape of individual cells changes from biconcave discs in (a) to more spheroidal shapes in (b) and (c). In addition, the collective aggregation in (c) is suggestive of rouleaux formation. (Image size: width × height = 1392 × 1040 pixels, 1 pixel = 6.45 μm). Field of view of microscope objective was 8.98 × 6.71 mm.

Further to examine potential complications caused by RBC shape changes and aggregation in the presence of added D-glucose, microscopy results from whole blood smears are shown in Fig. 6. Normal rat blood in 6a exhibits expected biconcave disc-like shapes of RBCs, seen as ~7-μm diameter circles with a central void in this transmission image. With addition of glucose (20 mM in Fig. 6b, 40 mM in Fig. 6c), deformation of individual erythrocytes into spheroidal shapes, and their multi-particle aggregation behavior are becoming evident. The former is a well know osmotic pressure effect, and the latter may be indicative of the rouleaux formation [7, 44–47]. Integration of our technique with photodynamic therapy can generate a new route to investigate cell death by analyzing the dynamic light scattering.

4. SUMMARY

We have used the temporal statistics of the OCT signal, specifically the characteristic decay times of its M-mode-derived autocorrelation functions, to study the viscosity of three different types of static liquid phantoms and bodily fluids (water, plasma and whole blood). The modulation of viscosity by the addition of D-glucose was investigated, motivated by our interest to determine the potential utility of speckle-variance OCT imaging for non-invasive D-glucose monitoring in diabetic patients. The determined viscosity values of water, plasma, and whole blood were in good agreement with the literature (where available), and showed the expected increasing trend with increasing D-glucose content. While translational diffusion dynamics were sufficient to analyze OCT data from samples containing symmetrical PMS, both translational and rotational relaxations had to be considered for whole blood analysis. The quantification of whole blood measurements in the presence of added D-glucose was challenging and required further refinement, owing to the complex nature of the blood milieu (such as viscosity changes, irregular RBC shape and its alterations, exposure to air complications and possible RBC aggregations). The microscopic results were obtained to further examine the deformation and aggregation behavior of red blood cells. While encouraging, these initial results also underscore the considerable difficulties in quantifying the whole blood measurements, and suggest several avenues of pursuit for future work.

5. FUTURE WORK

The addition of D-glucose to blood not only changes plasma viscosity, but also alters the shape of the erythrocytes; both of these can affect resulting Browning motion and thus the OCT decorrelation times. To tease out the relative contributions of these competing effects, we will examine the Brownian motion dynamics of non-deformable asymmetrical particles (e.g., micro-discs with ~7 μm diameter and ~2 μm thickness). We will also investigate quantitative ways of incorporating the derived rotational decorrelation times τ_R's into the viscosity analysis. Another area to explore in the effect of blood flow (forced convection). Even in capillaries, with its slow velocity rates of ~tens of μm/s, shorter decorrelation rates are expected that would have to be reliably measured. Further, the expressions of Eqs. (3) and (4) would no longer hold in the presence of flow, so a new theoretical formalism would be needed. Building on such systematic studies, one can eventually envision a scenario where a blood vessel identified by Doppler (or speckle variance) OCT is further examined in M-mode, with ACF analysis yielding its viscosity value that is directly linked to D-glucose content.

Further, the OCT signal can be analyzed to measure and identify the boundaries between normal and diseased blood in diabetics in vitro and in vivo. There would be some limitations imposed by the attenuation of the signal from depth, hence analysis may be limited to the top layers of tissue. A solution to depth problem and further contrast increase is suggested by use of optical clearing effect of D-glucose. The permeability coefficient estimation can also be used by measuring OCT signal slope to identify the normal and abnormal behavior [49–51].

ACKNOWLEDGMENTS

This research was supported by Higher Education Commission Pakistan, Islamabad, Canadian Institutes of Health Research, and The Princess Margret Hospital Foundation, University Health Network, Toronto, Canada. The authors gratefully acknowledge Emily Chan for assistance with drawn blood samples.

REFERENCES

1. M. G. Ghosn, S. H. Syed, N. A. Befrui, M. Leba, A. Vijayananda, N. Sudheendran, and K. V. Larin, Laser Phys. **19**, 1272 (2009).
2. L. Longo, Laser Phys. Lett. **7**, 771 (2010).
3. O. K. Cho, Y. O. Kim, H. Mitsumaki, and K. Kuwa, Clin. Chem. **50**, 1894 (2004).
4. E. H. Yoo and S. Y. Lee, Sensors **10**, 4558 (2010).
5. M. Bonesi, D. Y. Churmakov, L. J. Ritchie, and I. V. Meglinski, Laser Phys. Lett. **4**, 304 (2007).
6. A. N. Dbinaa, A. Y. Nooraldeen, K. Murali, and P. K. Palanisamy, Laser Phys. **18**, 1212 (2008).
7. O. S. Zhernovaya, V. V. Tuchin, and I. V. Meglinski, Laser Phys. Lett. **5**, 460 (2008).
8. V. V. Lychagova, A. L. Kal'yanov, and V. P. Ryabukho, Opt. Spectrosc. **107**, 859 (2009).
9. B. Veksler, E. Kobzev, M. Bonesi, and I. Meglinski, Laser Phys. Lett. **5**, 236 (2008).
10. M. Atif, H. Ullah, M. Y. Hamza, and M. Ikram, Laser Phys. Lett. **8** (2011), DOI 10.1002/lapl.201110035.

11. X. Guo, Z. Y. Guo, H. J. Wei, H. Q. Yang, Y. H. He, S. S. Xie, G. Y. Wu, H. Q. Zhong, L. Q. Li, and Q. L. Zhao, Laser Phys. **20**, 1849 (2010).
12. H. Keen, Brit. J. Diab. Vasc. Disease **2**, 419 (2002).
13. R. O. Esenaliev, K. V. Larin, and I. V. Larina, Opt. Lett. **26**, 992 (2001).
14. K. V. Larin, M. S. Eledrisi, M. Motamedi, and R. O. Esenaliev, Diab. Care **25**, 2263 (2002).
15. M. Kinnunen, R. Myllylä, and S. Vainio, J. Biomed. Opt. **13**, 021111 (2008).
16. Q. L. Zhao, J. L. Si, Z. Y. Guo, H. J. Wei, H. Q. Yang, G. Y. Wu, S. S. Xie, X. Y. Li, X. Guo, H. Q. Zhong, and L. Q. Li, Laser Phys. Lett. **8**, 71 (2011).
17. A. Mariampillai, M. K. K. Leung, M. Jarvi, B. A. Standish, K. Lee, B. C. Wilson, A. Vitkin, and V. X. D. Yang, Opt. Lett. **35**, 1257 (2010).
18. A. Z. Freitas, D. M. Zezell, M. P. A. Mayer, A. C. Ribeiro, A. S. L. Gomes, and N. D. Vieira, Jr., Laser Phys. Lett. **6**, 896 (2009).
19. K. K. Bizheva, A. M. Siegel, and D. A. Boas, Phys. Rev. E **58**, 7664 (1998).
20. A. Wax, C. Yang, R. R. Dasari, and M. S. Feld, Appl. Opt. **40**, 4222 (2001).
21. B. J. Berne, and R. Pecora, *Dynamic Light Scattering with Applications to Chemistry, Biology, and Physics* (Dover, Mineola, New York, 2000).
22. V. V. Sapozhnikova, R. V. Kuranov, I. Cicenaite, R. O. Esenaliev, and D. S. Prough, J. Biomed. Opt. **13**, 021112 (2008).
23. D. Chorvat, Jr. and A. Chorvatova, Laser Phys. Lett. **6**, 175 (2009).
24. B. Neu, R. Wenby, and H. J. Meiselmany, Biophys. J. **95**, 3059 (2008).
25. S. Prahl, http://omlc.ogi.edu/calc/mie_calc.html.
26. H. Ullah, M. Atif, S. Firdous, M. S. Mehmood, M. Ikram, C. Kurachi, C. Grecco, G. Nicolodelli, and V. S. Bagnato, Laser Phys. Lett. **7**, 889 (2010).
27. Hafeez-Ullah, M. Atif, S. Firdous, M. S. Mehmood, M. Y. Hamza, M. Imran, G. Hussain, and M. Ikram, Opt. Spectros. **110**, 313 (2011).
28. A. A. Alekhin, A. A. Ionin, S. E. Kozhushko, I. M. Kourylyova, S. I. Kudryashov, K. K. Kuz'min, V. G. Likhvansteva, M. V. Samoylov, L. V. Seleznev, D. V. Sinttsyn, and S. D. Zakharov, Laser Phys. Lett. **7**, 463 (2010).
29. Y. L. Jin, J. Y. Chen, L. Xu, and P. N. Wang, Phys. Med. Biol. **51**, N371 (2006).
30. A. Mariampillai, B. A. Standish, E. H. Moriyama, M. Khurana, N. R. Munce, M. K. K. Leung, J. Jiang, A. Cable, B. C. Wilson, I. A. Vitkin, and V. X. D. Yang, Opt. Lett. **33**, 1530 (2008).
31. R. K. Manapuram, V. G. R. Manne, and K. V. Larin, Laser Phys. **18**, 1080 (2008).
32. A. Mariampillai, *Development of a High Resolution Microvascular Imaging Toolkit for Optical Coherence Tomography*, PhD Thesis (Departm. of Med. Biophys., University of Toronto, 2010).
33. R. K. Manapuram, S. A. Baranov, V. G. R. Manne, N. Sudheendran, M. Mashiatulla, S. Aglyamov, S. Emelianov, and K. V. Larin, Laser Phys. Lett. **8**, 164 (2011).
34. N. Sudheendran, S. H. Syed, M. E. Dickinson, I. V. Larina, and K. V. Larin, Laser Phys. Lett. **8**, 247 (2011).
35. AxioObserver, http://www.aomf.ca/axioobserver.html, (2010).
36. H. Bai, P. Chen, H. Fang, L. Lin, G. Q. Tang, G. G. Mu, W. Gong, Z. P. Liu, H. Wu, H. Zhao, and Z. C. Han, Laser Phys. Lett. **8**, 78 (2011).
37. M. Brczinski, *Optical Coherence Tomography Principles and Applications* (Elsevier, San Diego, 2006).
38. A. Roggan, M. Friebel, K. Dorschel, A. Hahn, and G. Muller, Proc. SPIE (1998).
39. http://www.thermexcel.com/english/tables/eau_atm.htm.
40. V. R. N. Telisa, J. Telis-Romeroa, H. B. Mazzottia, and A. L. Gabasb, Int. J. Food Prop. **10**, 185 (2007).
41. S. Kim, S. Yang, and D. Lim, J. Mech. Sci. Tech. **23**, 868 (2009).
42. N. A. Dobrovol'skii, Y. M. Lopukhin, A. S. Parfenov, and A. V. Peshkov, Biomed. Eng. **31**, 140 (1997).
43. http://www.epakmachinery.com/products/viscosity-chart.
44. G. Barshtein, I. Tamir, and S. Yedgar, Eur. Biophys. J. **27**, 177 (1998).
45. A. A. Bednov, E. V. Savateeva, and A. A. Oraevsky, Proc. SPIE **4960**, 21–29 (2003).
46. T. W. Secom, B. Styp-Rekowsk, and A. R. Pries, Ann. Biomed. Eng. **35**, 755 (2007).
47. R. Skalak, P. R. Zarda, K. M. Jan, and S. Chien, Biophys. J. **35**, 771 (981).
48. L. Liu, A. W. N. Leung, X. S. Xia, D. Q. Bai, H. D. Lin, and C. S. Xu, Laser Phys. Lett. **8**, 150 (2011).
49. S. G. Proskurin and I. V. Meglinski, Laser Phys. Lett. **4**, 824 (2007).
50. H. Q. Zhong, Z. Y. Guo, H. J. Wei, C. C. Zeng, H. L. Xiong, Y. H. He, and S. H. Liu, Laser Phys. Lett. **7**, 315 (2010).
51. H. Q. Zhong, Z. Y. Guo, H. J. Wei, J. L. Si, L. Guo, Q. L. Zhao, C. C. Zeng, H. L. Xiong, Y. H. He, and S. H. Liu, Laser Phys. Lett. **7**, 388 (2010).